ELSEVIER

Contents lists available at ScienceDirect

Geothermics

journal homepage: www.elsevier.com/locate/geothermics



Analytical solutions to evaluate the geothermal energy generation potential from sedimentary-basin reservoirs

Daniel T. Birdsell ^{a,e}, Benjamin M. Adams ^a, Paromita Deb ^{a,*}, Jonathan D. Ogland-Hand ^a, Jeffrey M. Bielicki ^{b,f}, Mark R. Fleming ^c, Martin O. Saar ^{a,d}

- ^a Geothermal Energy and Geofluids Group, Department of Earth Sciences, ETH Zurich, Zurich, Switzerland
- b Department of Civil, Environmental, and Geodetic Engineering, The Ohio State University, Columbus, OH, USA
- ^c Department of Mechanical Engineering, Milwaukee School of Engineering, Milwaukee, WI, USA
- ^d Department of Earth and Environmental Sciences, University of Minnesota, Minneapolis, MN, USA
- e Neptune & Company, Inc., Denver, Colorado, USA
- f John Glenn College of Public Affairs, The Ohio State University, Columbus, OH, USA

ARTICLE INFO

Keywords: Sedimentary geothermal Electricity generation potential Porous media analytical solutions Electric power generation Reservoir impedance Geothermal reservoir heat depletion Wellbore heat loss

ABSTRACT

Sedimentary basins are attractive for geothermal development due to their ubiquitous presence, high permeability, and extensive lateral extent. Geothermal energy from sedimentary basins has mostly been used for direct heating purposes due to their relatively low temperatures, compared to conventional hydrothermal systems. However, there is an increasing interest in using sedimentary geothermal energy for electric power generation due to the advances in conversion technologies using binary cycles that allow electricity generation from reservoir temperatures as low as 80 °C. This work develops and implements analytical solutions for calculating reservoir impedance, reservoir heat depletion, and wellbore heat loss in sedimentary reservoirs that are laterally extensive, homogeneous, horizontally isotropic and have uniform thickness. Reservoir impedance and wellbore heat loss solutions are combined with a power cycle model to estimate the electricity generation potential. Results from the analytical solutions are in good agreement with numerically computed reservoir models. Our results suggest that wellbore heat loss can be neglected in many cases of electricity generation calculations, depending on the reservoir transmissivity. The reservoir heat depletion solution shows how reservoir temperature and useful lifetime behave as a function of flow rate, initial heat within the reservoir, and heat conduction from the surroundings to the reservoir. Overall, our results suggest that in an exploratory sedimentary geothermal field, these analytical solutions can provide reliable first order estimations without incurring intensive computational costs.

1. Introduction

Geothermal energy is a steady and dispatchable power generation source with a low carbon footprint. Depending on the temperature and enthalpy of the geothermal heat extraction fluid, geothermal energy can be used for direct applications, such as heating and cooling or for electricity generation. Geothermal resources from high temperature ($T > 180\,^{\circ}\text{C}$) hydrothermal reservoirs of volcanic origin are generally used for electricity generation, whereas medium- to low-temperature resources ($T < 180\,^{\circ}\text{C}$) are predominantly used for direct purposes, such as district heating, heating of greenhouses and balneological applications (Huenges, 2016; Moeck et al., 2019).

Over the past decades, however, numerous sedimentary basins have been investigated to assess their electric power generation potential such as the Molasse basin (Northern Alpine Foreland Basin), the Western Canadian foreland basin, the Upper Rhine Graben, and the North German basin, to name a few (Clauser, 2006; Agemar et al., 2014; Banks and Harris, 2018). Despite relatively low reservoir temperatures, electricity can be generated from such sedimentary formations by employing binary cycle energy conversion techniques, such as an Organic Rankine Cycle (ORC) or a Kalina cycle (Colonna et al., 2015; Arslan, 2011). In the binary cycle process, a working fluid, with a lower boiling point, is used to generate steam from the produced reservoir fluid at the land surface at temperatures as low as 85 °C (Moya et al., 2021). In Tartière and Astolfi (2017), the authors present a detailed analysis on the evolution,

^{*} Corresponding author.

E-mail address: pardeb@ethz.ch (P. Deb).

Nomenclature		r_1, r_2	distance from well to equipotential line (Section 2.1.3)		
		t	time		
A_c	cross-sectional area	t_d	dimensionless time		
A_{res}	conduction area of reservoir	x	cartesian horizontal spatial coordinate		
D	well diameter	x_0	location of well/porous media interface		
L	well spacing	Z	vertical spatial coordinate		
M	source-sink strength	Γ	non-dimensional temperature		
P	fluid pressure	ΔP	pressure difference in the reservoir between the injection		
Q_{Loss}	heat exchange from wellbore to surroundings		well and the midpoint between the injection and		
T_e	background geothermal temperature		production well		
T_{inj}	injection temperature	ΔP_{tot}	pressure difference in the reservoir between the injection		
T_r	reservoir temperature		well and the production well		
T_w	well wall temperature	ΔP_{Loss}	frictional losses in well		
q	Darcy velocity	β	Wellbore heat transfer factor		
V_{res}	volume of reservoir	\in	heat depletion term		
а	equivalent radius of the reservoir	θ	angle of rotation in radial coordinates		
a_A	area-based equivalent radius	κ	permeability		
a_V	volume-based equivalent radius	λ	inverse of the product of the contact resistance and the		
b	reservoir thickness		thermal conductivity		
c_{eff}	specific heat capacity of rock/water mixture	μ	fluid viscosity		
CFluid	working fluid specific heat capacity	$\overline{\mu}$	effective fluid viscosity in reservoir		
e	Euler's number	ξ	parameter that accounts for heat capacity inside and		
h	enthalpy		outside reservoir. Typically, $\xi = 3$ (see Section2.3).		
k_{eff}	effective thermal conductivity of saturated fluid/rock	ρ	fluid density		
9))	mixture	$ ho_{ ext{eff}}$	density of rock/water mixture		
ṁ	mass flow rate (general)	$\overline{\overline{\rho}}$	effective fluid density in reservoir		
\dot{m}_{tot}	total mass flow rate through well	φ	stream potential		
r	radial horizontal spatial coordinate	ω	thermal diffusivity of fluid/rock mixture		
r_0	well radius	-			

current installed capacity and growth potential of the ORC market. Few examples of ORC plants include the Neustadt-Glewe demonstration power plant in Germany, which was based on the ORC technology, utilizing a sandstone reservoir in the North-German sedimentary basin (Siebt et al., 2005). In the region of Munich, Germany, several geothermal power plants are in operation, which provide direct heat for district heating in the winter and electricity in the summer, extracting energy from the porous limestones and dolomites in the south-German Molasse basin (Lüschen et al., 2014). The Unterhaching geothermal power plant in this region was the first Kalina cycle based geothermal power plant in Europe, which operated until 2017 (Weber et al., 2021). Numerous other low- or medium-enthalpy geothermal projects are being developed in France, Germany, Austria and Switzerland, exploiting the main sedimentary basins such as the Upper Rhine Graben, the Molasse basin and the North German basin (Boissavy et al., 2019; Goldbrunner and Goetzl, 2019; Link and Minnig, 2022).

Sedimentary basins yield high potential to provide geothermal heat due to their: (a) widespread presence and frequent proximity to end users, (b) significant energy content (despite relatively low temperatures) due to their typical large size, compared to the rather small-scale, artificially generated Enhanced Geothermal System (EGS) reservoirs, and (c) often high natural transmissivities (i.e. low reservoir impedances) at least at moderate depths of a couple of kilometers. Furthermore, sedimentary basin reservoirs typically do not require hydraulic stimulation, in contrast to EGS, thereby significantly reducing the risk of inducing seismicity (Ge and Saar, 2022). However, electric power generation from such low-enthalpy sedimentary basin geothermal systems is relatively new, compared to electricity generation from high-enthalpy geothermal systems, which have been widely studied (e.g. Minissale, 1991; Langella et al., 2017; Deb et al., 2020). In addition to binary cycles, another approach to generating electric power from low-enthalpy sedimentary basin reservoirs is the use of subsurface carbon dioxide (CO₂) in so-called CO₂-Plume Geothermal (CPG) power plants

(Randolph and Saar, 2011). The use of CO₂ results in an approximate doubling of the thermal, and thus electric, energy production rate, compared to water, and enables direct placement of a CO₂-turbine in the single power loop, so that a binary cycle is not needed (Adams et al., 2014, 2015, 2021; Ezekiel et al., 2022). However, in this work, we focus on indirect binary cycle process using R245fa as a secondary working fluid. It is important to note here that R245fa belongs to a group of hydrofluorocarbons that has a high global warming potential (GWP) (Dawo et al., 2021). Alternatively, working fluids such as R1233zd(E) and R1224yd(Z) have similar thermophysical properties as R245fa but lower GWP values and are considered as potential drop-in replacement for R245fa in the future ORC plants (Eyerer et al., 2016, 2019). In this study, we use R245fa as the working fluid because this is the currently available commercial technology for power production and furthermore, we compare the results of this study with the numerical simulations performed in Adams et al. (2015), where R245fa is the working fluid. We use analytical methods to evaluate the electricity generation potential from sedimentary basin reservoirs without implementing computationally expensive reservoir simulation. Analytical models are typically easier to apply than numerical solutions and tend to have fewer degrees of freedom, reducing the likelihood of human error. Being computationally inexpensive, analytical models can be used to explore large parameter spaces and to perform sensitivity analyses. Analytical models have been used in many subsurface applications for first-order estimations and pre-screening evaluations such as geologic CO2 sequestration (Nordbotten and Celia, 2012), groundwater remediation (Bakker and Strack, 1996; Strack, 1999) and geothermal reservoir development (Birdsell et al., 2021). However, analytical approaches rely on simplified assumptions and approximations, making them often less suitable for solving complex geological problems. Numerical simulators, on the other hand, can handle problems with more complex geometries, heterogeneities, and coupled physics (e.g., thermo-hydro-mechanicalreservoir simulation). Numerical models may relax the assumptions

and approximations that some analytical solutions require, making them suitable for applications where such simplifications are not justified. On the other hand, increasingly complex numerical models can require large amounts of input data for parameter specification, meshing choices, and setup of boundary and initial conditions. Given these tradeoffs between analytical and numerical methods, no method is always more favorable, precise, or accurate, compared to the other.

When exploring geothermal fields with little to no data that characterize the subsurface, initial calculations are typically based on assumptions that the reservoir is homogeneous and isotropic. In such greenfields, analytical methods might provide sufficiently reasonable first-order approximations of the geothermal energy production potential, which are comparable to the results of the numerical models. We test this hypothesis by comparing results from both approaches, i.e., employing both analytical and numerical reservoir calculations in sedimentary reservoirs that are laterally extensive, homogeneous, horizontally isotropic and have uniform thicknesses. Hence, the objectives of our work are to:

- i introduce analytical solutions for assessing the sedimentary reservoir impedance, reservoir heat depletion over time and wellbore heat loss.
- ii couple the analytical solutions for reservoir impedance and wellbore heat loss with a power cycle model, including thermodynamic calculations for turbine(s), cooler(s), condenser(s), boiler(s), and pump (s), to estimate the electric power generation potential,
- iii analyze the reservoir heat depletion as an indicator of how the electric power generation decreases over a project lifetime, and
- iv compare the estimates from analytical solutions with the results from numerical models to clarify and further demonstrate the advantages and disadvantages of the two methods for representing the subsurface.

While the equations in objective (i) are not entirely novel, a summary and comparison of these analytical equations is valuable and important to understand the method's applicability to sedimentary geothermal systems. More importantly, the coupling of analytical reservoir equations with a power cycle model in objective (ii) and the ability to investigate objective (iii) are novel contributions. Further, the resultant comparison of electricity generation using both analytical and numerical reservoir equations in (iv), is also novel. The paper is organized as follows: In Section 2, we introduce the analytical solutions that describe the reservoir behavior and recapitulate the numerical reservoir simulator and the power cycle model from previous work (Adams et al., 2015, 2021). In Section 3, we compare the results from the analytical model with those from the numerical model with respect to estimated power generation and operational reservoir lifetime. Section 4 presents our conclusions.

2. Methods

As mentioned earlier, we implement analytical reservoir solutions coupled with a power cycle model to calculate electric power generation and to gain knowledge concerning the operational lifetime of a sedimentary-basin geothermal reservoir. The heat and electric power generation rates are proportional to the flow rate and temperature of the produced fluid. Therefore, in Sections 2.1 and 2.2, we provide analytical solutions for the reservoir impedance and wellbore heat loss. The operational lifetime of the reservoir is related to the reservoir heat depletion rate, as power generation decreases with reservoir temperature. Therefore, in Section 2.3, we provide an analytical solution for reservoir heat depletion. In Section 2.4 and 2.5, we review the numerical reservoir simulator and the power cycle model from Adams et al. (2015), which remain mostly unchanged in this work.

The key simulation parameters and assumptions are given in Table 1 and are consistent with the base case scenario presented in Adams et al.

Table 1Model assumptions and parameters.

Parameter	Value
Reservoir parameters	
Well pattern	1 km ² Inverted 5-spot
Primary geothermal fluid	Water
Secondary ORC fluid	R245fa
Well diameter (D)	0.41 m
Well spacing (L)	707 m
Geologic temperature gradient	35 °C/km
Surface temperature	15 °C
Reservoir depth	2.5 km
Injection temperature (T_{inj})	22 °C
Far-field temperature (T_e)	102.5 °C
Flow rate (\dot{m})	100 kg/s (for the reservoir heat depletion
	calculations in Sections 2.3 and 3.3.)
	Maximized power (for the power generation calcs
	in Sections 2.5 and 3.2.)
Reservoir pressure	Hydrostatic
Permeability (κ)	5.10^{-14} m^2
Reservoir thickness (b)	300 m
Thermal conductivity of saturated media	2.1 W/m- °C
Density of saturated media (ρ_{eff})	2485 kg/m ³
Specific heat capacity of saturated media (c_{eff})	1320 J/kg- °C
Thermal conductivity of saturated media (k_{eff})	2.1 W/m- °C
Other reservoir assumptions	Laterally extensive, horizontal, homogeneous,
•	horizontally isotropic, uniform thickness
Power Cycle Generation Model I	
ORC isentropic turbine	80%
efficency (assumed)	
Pump efficiency (assumed)	90%
Ambient mean annual air	15 °C (Dallas,TX)
temperature	
Cooling or condensing tower approach temperature	7 °C
Cooling or condensing tower type	Wet, closed circuit
Pinch point temperature	7 °C

(2015) and are justified in that reference. For example, the 35 $^{\circ}$ C/km geothermal temperature gradient is approximately equal to the average value for the continental crust of the Western United States (Nathenson and Guffanti, 1988). For the sake of brevity, we do not repeat all the justification here. However, it is important to note that we assume the reservoir is horizontal, homogenous, horizontally isotropic, has a uniform thickness, and is bounded by impermeable aquicludes above and below.

2.1. Reservoir impedance analytical solutions

Reservoir impedance is defined as the pressure difference between an injection well and a production well divided by the mass flow rate, i.e., $\Delta P_{tot}/\dot{m}_{tot}$ where ΔP_{tot} is the pressure difference in the reservoir between the injection well and the production well and \dot{m}_{tot} is the total flow rate through the injection well. All other parameters remaining the same, low reservoir impedances enable higher flow rates, leading to increases in thermal and electric power generation rates.

We analyze two well patterns: an inverted 5-spot tessellated well pattern developed field (TDF) and an isolated doublet (ID). A TDF is a geothermal field that contains a repeating pattern of wells in a laterally extensive reservoir. An example of a TDF is the inverted 5-spot well pattern shown in Fig. 1, employed in many previous reservoir simulations (e.g., Randolph and Saar, 2011; Adams et al., 2015, 2021). An inverted 5-spot well pattern consists of four equidistant production wells on the corners of a square with one injection well in the center of the square. We assume that one quarter of the fluid mass from each production well is injected back into the central injection well to maintain

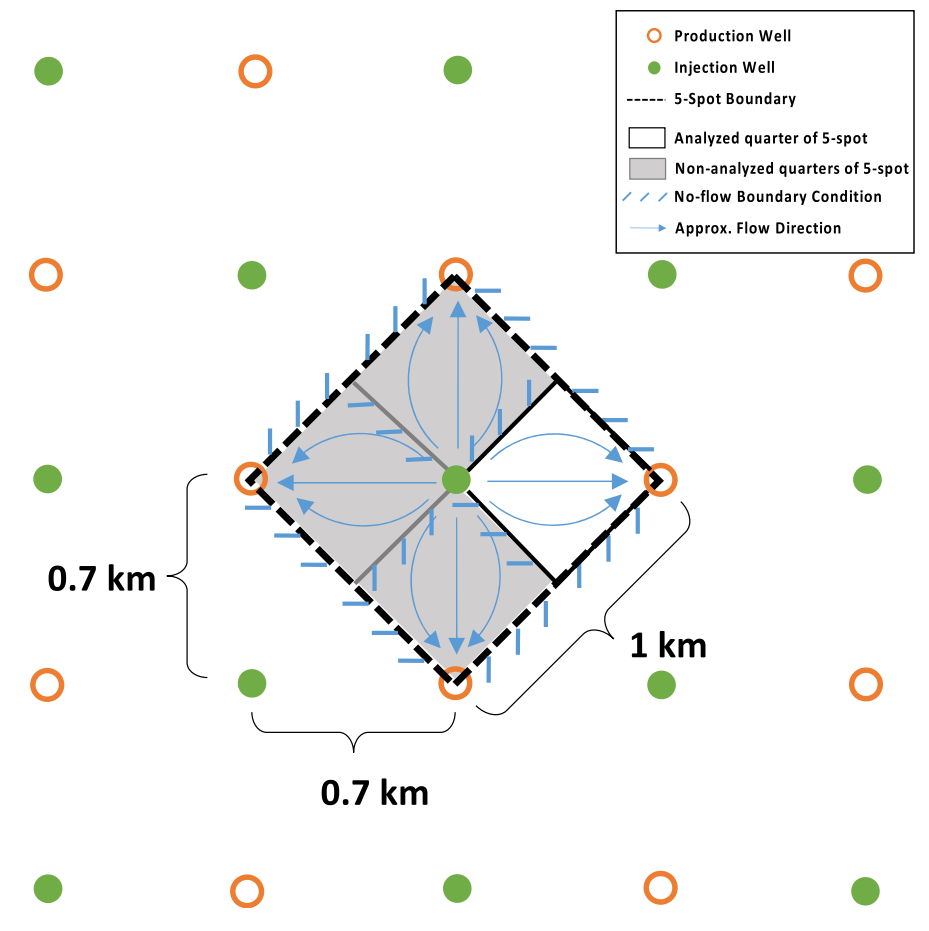


Fig. 1. Schematic of an inverted 5-spot tessalated well pattern developed field (TDF). Within the inverted 5-spot TDF pattern, one quarter (i.e., quadrant) is analyzed (white box with black outline). No-flow boundary conditions (blue dashes) are utilized to separate the analyzed quarter of the inverted 5-spot from: 1) the other, non-analyzed quarters (or quadrants) of the inverted 5-spot (gray box with dark gray outlines) and 2) the other inverted 5-spots. These no-flow boundaries are valid due to the symmetry of the fluid flow direction (indicated by the blue arrows) and are commonly invoked (e.g. Pruess, 2006).

reservoir pressure; the remaining produced fluid mass is injected into neighboring injection wells. In total, the fluid mass injected into any injection well is thus the same as the fluid mass extracted from any production well. When analyzing an inverted 5-spot TDF, we assume that there are many inverted 5-spots (as shown in Fig. 1), and we analyze an internal inverted 5-spot that is far from the boundaries of the well field, which allows us to use symmetry to simplify boundary conditions and perform calculations for only one quarter (i.e., one quadrant) of an inverted 5-spot, as depicted in Fig. 1 and as used previously (e.g., Randolph and Saar, 2011; Adams et al., 2015, 2021). Since only one quarter of the 5-spot is analyzed, only one-quarter of the injection screen is analyzed, and therefore only one quarter of the total injection volume is considered in the derivations in Sections 2.1.1 and 2.1.3. As Fig. 1 shows, hydrologically, there is no flow laterally to adjacent inverted 5-spot patterns and no flow laterally to the remaining three quarters of the 5-spot pattern (Randolph and Saar, 2011; Adams et al., 2015, 2021). Furthermore, there is no flow vertically because of the (assumed) impermeable units above and below the reservoir. These boundary conditions are valid under the assumptions of a horizontal, homogeneous, isotropic, laterally extensive reservoir with repeating adjacent 5-spot TDF; the boundary conditions and the approximate flow pattern are depicted in Fig. 1.

While the inverted 5-spot TDF represents a mature field, many geothermal fields will start with a single injection-production well pair. We define an isolated doublet (ID) as an injection-production well pair with non-zero well spacing, located far from any other wells, so that there is no external hydraulic or thermal influence. Therefore, we analyze IDs and inverted 5-spot TDFs, which act as bounding cases in a

geothermal field's lifetime. In our analysis, the well spacing between an injection and a production well is assumed to be 707 m for both the ID and the inverted 5-spot TDF, i.e. half of the diagonal of a $1 \times 1 \text{ km}^2$ inverted 5-spot well pattern (Fig. 1).

We provide four analytical solutions that integrate Darcy's equation to give the reservoir impedance. The difference between each approach comes from the definition of the cross-sectional area within Darcy's equation, which is described in more detail in Sections 2.1.1-2.1.4 below. Pressure contours for each approach are shown in Fig. 2, and the flow direction is perpendicular to each pressure contour. The first approach (Section 2.1.1) uses a cartesian coordinate system to define the cross-sectional area, which honors the flow behavior that should be parallel to the x-axis at the midpoint in between an injection and a production well in a 5-spot (see "TDF-Cartesian" in Fig. 2a). The second approach (Section 2.1.2) applies primarily to the ID and uses a radial coordinate system, which honors the radial behavior of flow near an injection or a production well (see "TDF-Radial" in Fig. 2a or "ID-Radial" in Fig. 2b). The third approach (Section 2.1.3) is a hybrid method, which implements the best of the first two approaches, such that the radial fluid flow near either well and the lateral fluid flow at the midpoint between the two wells are both honored for the 5-spot TDF (see "TDF-Hybrid" in Fig. 2a). The final approach (Section 2.1.4 and "ID-Potential" in Fig. 2b) applies to the ID and uses a method that is based on the potential function and streamlines to improve the "ID-Radial" solution.

It is important to note that all derivations in Section 2.1 are onedimensional, rely on average fluid properties, and assume a uniform fluid velocity profile through a cross-sectional area. Thus, the solutions do not account for fluid flow deviations from these fluid flow patterns

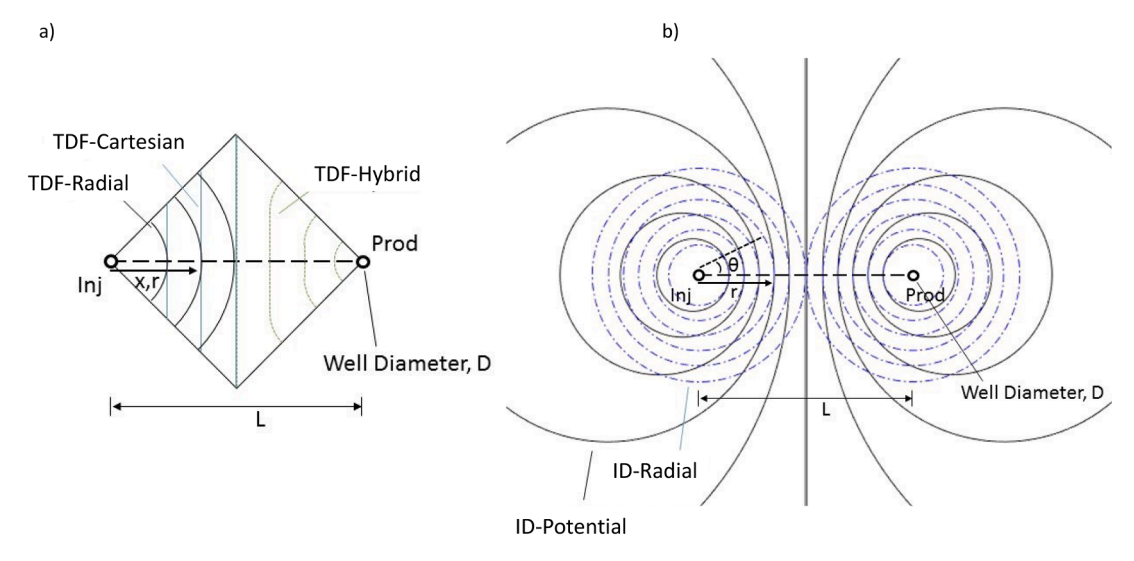


Fig. 2. Pressure contours for (a) one-quarter of a 5-spot TDF and (b) an ID in plan view, where "Inj" indicates the injection well and "Prod" indicates the production well. These pressure contours correspond to the cross-sectional area divided by the reservoir thickness for the solutions derived in Section 2.1.1–2.1.4 and vary based on the method used (e.g., "ID-Radial"; "ID-Potential"; "TDF-Cartesian"; "TDF-Radial"; or "TDF-Hybrid"). Note that θ is the angle of rotation arround the well and is utilized in Section 2.1.4 for the "ID-Potential" solution.

(Fig. 2), heterogeneities, or buoyancy forces. However, the solutions do, at a minimum, provide an order-of-magnitude approximation of the geothermal reservoir behavior under production. Due to the symmetry of the inverted 5-spot TDF, only one quarter of the system is analyzed in Sections 2.1.1 and 2.1.3. All the sides in Fig. 2a can be treated as no-flux boundary conditions, as discussed earlier in this section.

2.1.1. 5-spot tessellated, developed field (TDF) in Cartesian coordinates

The one-dimensional Darcy equation for horizontal flow can be expressed in Eq. (1), where P is the fluid pressure from both elevation and pressure head, μ is the dynamic viscosity of the fluid, q is the Darcy velocity (specific discharge), κ is the permeability, and x is distance in the direction of fluid flow.

$$dP = -\frac{\mu \cdot q}{\kappa} dx \tag{1}$$

The continuity equation is shown in Eq. (2), where the mass flow rate, \dot{m} , is equal to the product of fluid density, ρ , the cross-sectional area, A_c , and the Darcy velocity, q. Here, \dot{m} is the flow rate through the portion of the injection well that is analyzed. Therefore, in the solutions for the 5-spot TDF in Sections 2.1.1 and 2.1.3, where only one quarter of the injection well screen is analyzed, \dot{m} equals only one-fourth of the total mass flow rate, \dot{m}_{tot} . In contrast, the whole circumference of the well screen is analyzed in the ID solutions in Sections 2.1.2 and 2.1.4, so that \dot{m} equals \dot{m}_{tot} in those sections.

$$\dot{m} = \rho \cdot A_c \cdot q \tag{2}$$

Eq. (2) is substituted into Eq. (1), yielding Eq. (3).

$$dP = -\frac{\mu}{\rho} \frac{\dot{m}}{\kappa \cdot A_c} dx \tag{3}$$

For a one-quarter domain of a 5-spot configuration, the x-axis is aligned with the line between the injection and production wells (see Fig. 2a). The cross-sectional area, A_c , through which Darcy fluid flow occurs in the reservoir is given by Eq. (4), where b is the reservoir thickness. The lines "TDF-Cartesian" in Fig. 2a indicate the cross-sectional area, divided by the reservoir thickness, b.

$$A_c = 2 \cdot x \cdot b \tag{4}$$

By combining Eqs. (3) and 4 and integrating from the interface between the well and the porous medium (i.e., the outside of the casing), x_0 , to the midpoint between the two wells, L/2, yields Eq. (5), where L is

the distance between the injection and the production wells (i.e., the well spacing). Integration of Eq. (5) yields Eq. (6), where ΔP is the pressure decrease from the injection well to the midpoint. The dynamic viscosity, $\overline{\mu}$, and the density, $\overline{\rho}$, are average values for the entire

$$\int dP = -\frac{\overline{\mu}}{\overline{\rho}} \frac{\dot{m}}{2 \cdot \kappa \cdot b} \int_{-\infty}^{\frac{L}{2}} \frac{1}{x} dx \tag{5}$$

$$\Delta P = \frac{\overline{\mu}}{\overline{\rho}} \frac{\dot{m}}{2 \cdot \kappa \cdot \dot{b}} \ln \left(\frac{L}{2 \cdot x_0} \right) \tag{6}$$

To find the total fluid pressure difference in the reservoir between the injection well and the production well, ΔP_{tot} , Eq. (6) must be doubled, as it estimates the pressure loss from the injection well to the mid-point between the injection and the production wells. The fluid pressure continues to drop at the same rate going from the midpoint to the production well. As a result, this doubling cancels out the 2 in the denominator of Eq. (6).

Also, the well perimeter in this one-dimensional Cartesian space is a square, where each side of the square has a length of $2 \cdot x_0$. Thus, it is possible to equate the perimeter of the square with the circumference of a circle with a diameter, D, which will represent the diameter of the well, to yield Eq. (7).

$$\pi \cdot D = 4 \cdot (2 \cdot x_0) \tag{7}$$

Substituting Eq. (7) into Eq. (6) yields the pressure difference as a function of the well diameter, D. This equation is valid for all quadrants of the inverted 5-spot well pattern, and the total flow rate through the well is $\dot{m}_{tot} = 4\dot{m}$, due to the symmetry of the problem. We express the reservoir impedance in terms of ΔP_{tot} and \dot{m}_{tot} in Eq. (8), which facilitates comparisons with other solutions in Section 2.1. Note that the reservoir impedance is inversely proportional to the reservoir transmissivity, κb , which is the product of reservoir permeability and thickness.

$$\frac{\Delta P_{tot}}{\dot{m}_{tot}} = \frac{\overline{\mu}}{\overline{\rho}} \frac{1}{4 \cdot \kappa \cdot b} \ln \left(\frac{4 \cdot L}{\pi \cdot D} \right)$$
 (8)

2.1.2. Isolated doublet (ID) in radial coordinates

We use an approach similar to that in Section 2.1.1 to solve for the reservoir impedance of an isolated doublet (ID), which is an injection-

production pair that is far from the influence of other wells (Fig. 2b). We assume that the fluid flow between the injection well and the production well is radial and uniform in all directions, up to a radius of L/2. For this injection-production well pair, we use radial coordinates and substitute dx = dr in Eq. (1). The cross-sectional area of flow is the product of the circumference at radius r and the reservoir thickness b (Eq. (9)). In one-dimensional radial coordinates, the well perimeter is a circle unlike one-dimensional Cartesian coordinates where the well perimeter is a square (Section 2.1.1). Hence, the cross-sectional area, divided by the reservoir thickness, is illustrated by the lines labeled "ID-Radial" in Fig. 2b.

$$A_c = 2 \cdot \pi \cdot r \cdot b \tag{9}$$

By combining Eqs. (3) and (9), we obtain Eq. (10), where r_0 is the well radius, which is analogous to x_0 in Section 2.1.1. Integration yields Eq. (11), which is the pressure difference from the well to the midpoint between the injection and the production wells.

$$\int dP = -\frac{\overline{\mu}}{\overline{\rho}} \frac{\dot{m}}{2 \cdot \pi \cdot \kappa \cdot b} \int_{r}^{\frac{L}{2}} \frac{1}{r} dr \tag{10}$$

$$\Delta P = \frac{\overline{\mu}}{\overline{\rho}} \frac{\dot{m}}{2 \cdot \pi \cdot \kappa \cdot b} \ln \left(\frac{L}{2 \cdot r_0} \right) \tag{11}$$

Eq. (11) is rearranged to include the reservoir impedance of a sourcesink pair (Eq. (12)), where the well radius is half the well diameter. Note that the flow rate, \dot{m} , is equal to \dot{m}_{tot} in this section because we use the entire circumference of the well, unlike in Section 2.1.1, where we analyzed one-quarter of the well circumference.

$$\frac{\Delta P_{tot}}{\dot{m}_{tot}} = \frac{\overline{\mu}}{\overline{\rho}} \frac{1}{\pi \cdot \kappa \cdot b} \ln \left(\frac{L}{D} \right) \tag{12}$$

The radial approach can also be used to derive the impedance of an inverted 5-spot TDF, where the impedance calculated for the "ID-Radial" is the same as that of the "TDF-Radial" (i.e. Eq. (12) also applies to an inverted 5-spot TDF, analyzed with radial coordinates (Fig. 2a). This can be derived following the same approach as in Section 2.1.1, except the lower bound of the integration in Eq. (5) is then D/2 and $A_c = \pi rb/2$. Since we show a similar derivation in this section (i.e., Section 2.1.2), it is not repeated.

Note that for large values of L/D, the reservoir impedance of the "ID-Radial" solution (Eq. (12)) is larger than the reservoir impedance of an inverted 5-spot TDF-Cartesian (Eq. (8)) by a factor of 4 $/\pi$. This 27% difference is due to the 27% smaller sweep area of the "ID-Radial" and the "TDF-Radial" solutions, compared to the "TDF-Cartesian" solution. Thus, in Section 2.1.4, we use the potential functions to include the entirety of the reservoir area for an ID.

2.1.3. 5-Spot tessellated, developed field (TDF), hybrid

In a 5-spot "TDF-Hybrid", the cross-sectional area, divided by the reservoir thickness, is best represented by a circular arc near the well because fluid flow is radially away from the injection well (see "TDF-Radial" in Fig. 2a). However, at the midpoint between the wells, the cross-sectional area, divided by the reservoir thickness, is best represented by a line that is perpendicular to the x-coordinate due to the symmetry in the 5-spot TDF (see "TDF-Cartesian" in Fig. 2a). We define a hybrid cross-sectional area in Eq. (13) that honors the radial flow near either well and the cartesian flow at the midpoint between the wells. The hybrid area, divided by the reservoir thickness, is illustrated in Fig. 2a by the lines labeled "TDF Hybrid."

$$A_{c} = \frac{2b}{\frac{L}{2} - x_{o}} \left(x^{2} \left(1 - \frac{\pi}{4} \right) + x \left(\frac{L\pi}{8} - x_{o} \right) \right)$$
 (13)

The same approach as shown in Sections 2.1.1 and 2.1.2 is used to find the reservoir impedance (Eq. (14)).

$$\frac{\Delta P_{tot}}{\dot{m}_{tot}} = \frac{\overline{\mu}}{\overline{\rho}} \frac{1}{\pi \cdot \kappa \cdot b} \ln \left(\frac{\pi}{4} \frac{L}{D} \right) \tag{14}$$

2.1.4. Isolated doublet (ID) with potential flow

The pressure potential curve surrounding an injection well or a production well does not have a constant radius, as is assumed in Section 2.1.2. Thus, to find a more precise solution for an ID, we integrate the distance of the potential curve surrounding the sink to obtain the cross-sectional area (Eq. (15)), where r_1 is the radius to the equipotential line from the sink and θ is the angle of integration around the well, as shown in Fig. 2.

$$A_c = b \cdot \int_0^{2\pi} r_1 \ d\theta \tag{15}$$

For source-sink potential flow, the stream potential, φ , is given by Eq. (16), where M is the source-sink strength, r_1 is the radial distance from the sink, and r_2 is the radial distance from the source (Stern 2006).

$$\varphi = -\frac{M}{2\pi} \ln \left(\frac{r_1}{r_2} \right) \tag{16}$$

The shortest streamline extends directly from the sink to the source and is shown as a dashed line in Fig. 2b. The potential along this streamline is given by Eq. (17), which is evaluated by applying $r_1 = r$ and $r_2 = L - r$.

$$\varphi = -\frac{M}{2\pi} \ln \frac{r}{L - r} \tag{17}$$

Equating Eqs. (16) and (17) yields Eq. (18), which provides the distances r_1 and r_2 along a line of constant potential as a function of L and r. Eq. (18) is solved for r_2^2 in Eq. (19).

$$\frac{r_2}{r_1} = \frac{L}{r} - 1 \tag{18}$$

$$r_2^2 = r_1^2 \cdot \left(\frac{L}{r} - 1\right)^2 \tag{19}$$

Using trigonometry, we find length r_2 as a function of r_1 and θ independent of the considerations of potential flow in Eq. (20)

$$r_2^2 = r_1^2 + L^2 - 2 \cdot L \cdot r_1 \cdot \cos\theta \tag{20}$$

Equating Eqs. (19) and (20), solving for r_1 , integrating according to Eq. (15), and assuming large values of L (i.e. $L\gg 1$) yields Eq. (21). The L>>1 assumption is likely valid for most of the sedimentary-basin geothermal fields that this paper pertains to because optimal well spacing is likely to be hundreds of meters (Adams et al., 2015).

$$A_c = \frac{2 \cdot \pi \cdot b}{\left(\frac{1}{r^2} - \frac{2}{Lr}\right)^{1/2}} \tag{21}$$

The denominator in Eq. (21) does not lend itself to simple integration. We thus approximate Eq. (21) with Eq. (22). This approximation preserves the anomaly occurring at r = L/2, where the cross-sectional area becomes infinite. At the midpoint between the injection well and the production well, the line of equal potential is tangent to the streamline, extending to infinity.

$$\left(\frac{1}{r^2} - \frac{2}{L \cdot r}\right)^{1/2} = \left(\frac{1}{r}\right)^{1/2} \cdot \left(\frac{1}{r} - \frac{2}{L}\right)^{1/2} \approx \left(\frac{1}{r} - \frac{2}{L}\right)$$
 (22)

Eqs. (21) and (22) are combined with Eq. (3) in radial space (dx = dr) and integrated using an approach similar to Eq. (10). The resulting reservoir impedance is given by Eq. (23), where e is Euler's number.

$$\frac{\Delta P_{tot}}{\dot{m}_{tot}} = \frac{\overline{\mu}}{\overline{\rho}} \frac{1}{\pi \cdot \kappa \cdot b} \left[\ln \left(\frac{L}{D \cdot e} \right) + \frac{D}{L} \right]$$
 (23)

The solution in Eq. (23) is similar to the solution in Eq. (12); i.e., the "ID, Potential" and the "ID, Radial" differ only by the factor of e within the natural logarithm. The D/L term is small for large values of L/D and can be neglected without much loss of precision. For well spacing to well diameter ratios of 1000 (i.e., L/D=1000), Eq. (23) provides a reservoir impedance value approximately 15% smaller than Eq. (12). This decreased impedance, using the "ID-Potential" method (Eq. (23)), is enabled by the infinite swept volume, whereas the "ID-Radial" solution (Eq. (12)) has a finite swept volume.

2.2. Wellbore heat loss analytical solution

Heat loss to the rock surrounding the wellbore is implemented using a semi-analytical approach. In each wellbore element that is numerically integrated (Adams et al., 2015), an analytical heat solution for a semi-infinite solid is applied from Zhang et al. (2011). This approach assumes that heat conduction only occurs radially to the far-field and that the wellbore wall temperature is constant with time.

Similar to Adams et al. (2015), the wellbore elements are evaluated numerically, with pressure (Eq. (24)) and energy (Eq. (25)) balances across each element, where Δz is the change in element elevation, ΔP_{Loss} is the pipe frictional loss, h is the enthalpy, Q_{Loss} is the heat exchange to the surroundings, \dot{m} is the fluid mass flow rate, and an "i" subscript indicates the value at the ith element. The pressure loss equation is identical to Adams et al. (2015), while the energy equation includes the new heat exchange term.

$$P_{i+1} = P_i - \rho_i \cdot g \cdot \Delta z - \Delta P_{Loss,i}$$
 (24)

$$h_{i+1} = h_i - g \cdot \Delta z - \frac{Q_{Loss,i}}{\dot{n}} \tag{25}$$

The heat loss is solved with Eq. (26) from Zhang et al. (2011), where k_{eff} is the effective thermal conductivity of the rock/water porous media complex, β is a non-dimensional, time-dependent factor for heat transfer, T_w is the well casing temperature, and T_e is the background, far-field temperature at depth, equal to the product of geologic temperature gradient and reservoir depth plus the mean annual surface temperature. It is assumed that the well casing and fluid heat transfer resistances are small compared to conduction through the rock and are thus negligible.

$$Q_{Loss,i} = \Delta_{z} \cdot 2 \cdot \pi \cdot k_{eff} \cdot \beta \cdot (T_{w,i} - T_{e,i})$$
(26)

The well casing temperature is an intermediate temperature between the wellbore fluid temperature and the far-field temperature. Without heat loss, the wellbore elements are assumed to be sufficiently long that the fluid temperature is in thermal equilibrium with the well casing. Thus, the well casing temperature, T_w , is assumed to be the resulting fluid temperature for an enthalpy of h_i and a pressure of P_i if the heat loss term in Eq. (25) were zero.

The dimensionless factor β is given by Zhang et al. (2011) as Eq. (27), where t_d is dimensionless time.

$$\beta = \begin{cases} (\pi \cdot t_d)^{-1/2} + \frac{1}{2} - \frac{1}{4} \left(\frac{t_d}{\pi}\right)^{\frac{1}{2}} + \frac{1}{8} t_d, & t_d \le 2.8\\ \frac{2}{\ln(4 \cdot t_d) - 1.16} - \frac{1.16}{(\ln(4 \cdot t_d) - 1.16)^2}, & t_d > 2.8 \end{cases}$$
(27)

The dimensionless time, t_d , is given in Eq. (28), where ω is the thermal diffusivity of the rock/fluid porous media complex and t is (dimensional) time.

$$t_d = \omega \frac{4 \cdot t}{D^2} \tag{28}$$

2.3. Reservoir heat depletion analytical solution

Recent work used numerical solutions to show how reservoir heat depletion affects electric power output (Adams et al., 2021). We adapt a

heat depletion analytical solution from Carslaw and Jager (1986) to estimate the sedimentary basin heat depletion. This approach is similar to that used by Zhang et al. (2011).

The reservoir is treated as a sphere with infinite thermal conductivity, which is situated within a semi-infinite medium at the background, far-field geothermal temperature. The temperature of the reservoir is (Carslaw and Jager, 1986):

$$T_r = \frac{-Q}{4\pi a_A k_{eff}} \in (t) + T_e, \tag{29}$$

where Q is the rate of heat removal from the reservoir, a is the equivalent radius of the reservoir, where its subscript is discussed in more detail later in this section, and \in is a function of time and parameters related to reservoir size, geometry, and thermal diffusivity.

The rate of heat removal from a reservoir is:

$$Q = -\dot{m}c_{Fluid}(T_{inj} - T_r),\tag{30}$$

where T_{inj} is the fluid injection temperature and c_{Fluid} is the working fluid's specific heat capacity. We assume that the heat extraction rate is constant (to be consistent with Eq. (29)) and we substitute Eq. (30) into Eq. (29). While Q will actually decrease with time as the reservoir temperature decreases (assuming a constant mass flow rate), Eq. (29) will give approximate values of reservoir temperature at early times, before the temperature declines are substantial. We are most interested in temperature depletion at these early times. For later times, when the temperature depletion is large, the solution to Eq. (29) will be conservative as it will rather overpredict temperature depletion.

With algebraic manipulation of Eqs. (29) and (30), a nondimensional reservoir temperature can be expressed as:

$$\Gamma = \frac{T_r - T_{inj}}{T_e - T_{inj}} = \left(\frac{\dot{m}c_{Fluid}}{4\pi a_A k_{eff}} + 1\right)^{-1}$$
(31)

where \in is defined as:

$$\epsilon = \frac{1 + a_V \lambda}{a_V \lambda} - \frac{2a_V^2 \xi^2 \lambda^2}{\pi} \int_0^\infty \frac{\exp\left(\frac{\omega u^2 t}{a_V^2}\right) du}{\left[\left(u^2 (1 + a_V \lambda) - \xi a_V \lambda\right)\right]^2 + \left[u^3 - \xi a_V \lambda u\right]^2} \tag{32}$$

where λ is the inverse of the product of the contact resistance between the reservoir and the surrounding rock/fluid complex and the thermal conductivity of the reservoir-surrounding rock/fluid complex, ξ has a value of three when the density and specific heat capacity of the reservoir are the same as the reservoir-surrounding rock (as we assume), and u is an integration variable.

As an aside, we note that the non-dimensional temperature in the absence of conduction is given by:

$$\Gamma = \frac{T_r - T_{inj}}{T_e - T_{inj}} = \left(\frac{t\dot{m}c_{Fluid}}{V_{res}\rho_{eff}c_{eff}} + 1\right)^{-1}$$
(33)

where V_{res} is the reservoir volume.

In the limit as λ approaches infinity, \in can be expressed more simply as:

$$\epsilon = 1 - \frac{2\xi^2}{\pi} \int_{0}^{\infty} \frac{\exp\left(\frac{\omega u^2 t}{a_V^2}\right) du}{(u^2 - \xi)^2 + (\xi u)^2} \tag{34}$$

Analytical solutions of \in exist for both early and late time (Carslaw and Jager, 1986). Nonetheless, we solve the integral in Eq. (34) numerically so that the solution covers all times that are relevant for geothermal development, including intermediate times that the analytical solutions do not represent well.

In the original Carslaw and Jager (1986) solution, a represents the radius of a sphere. However, since geothermal reservoirs are typically

not spherical, we find that careful specification of the equivalent radius can improve the solution. The equivalent radius could be specified to match the reservoir volume, a_V , or the surface area over which heat conduction occurs, a_A :

$$a_V = \left(\frac{3V_{res}}{4\pi}\right)^{\frac{1}{3}} \tag{35}$$

$$a_A = \sqrt{\frac{A_{res}}{4\pi}} \tag{36}$$

where A_{res} is the surface area of the reservoir exposed to heat conduction from the surroundings.

In separate comparisons to the numerical solution for reservoir heat depletion (see Section 2.4), we find that it is best to use the area-based equivalent radius outside of \in (i.e., in Eqs. (29) and (31)). This ensures that the temperature is correct as time approaches infinity because the late-time steady-state temperature occurs when the heat extraction rate is equal to the rate of conductive heat transfer into the reservoir. We use the volume-based radius for the calculation of \in (Eq. (34)), which ensures that the initial amount of heat in the reservoir is correctly accounted for.

2.4. Numerical simulations

We also perform numerical thermo-hydraulic reservoir simulations for comparisons with the analytical solutions. The simulations calculate reservoir impedance and the temperature at the production well with respect to time.

The simulations are performed with the reservoir simulator TOUGH2 with the Equation of State ECO2N module (Pruess 2004, 2005) and investigate one-eighth of a 5-spot TDF, similar to Adams et al. (2015). The input file and mesh (included in the Supplemental Information) are based on an example in the TOUGH2 manual (Pruess et al., 1999, Section 9.4), where we intentionally changed as little as possible. The mesh contains 36 elements, consistent with the TOUGH2 manual example and previous studies (Randolph and Saar, 2011; Adams et al., 2015). We apply fixed mass flow rate boundary conditions at the injection and production cells. We maintain the pressure at the corner node as the hydrostatic reservoir pressure by supplying constant fluid pressure as needed. Due to symmetry, there is no flux of heat or fluid across the vertical reservoir boundaries. There is also no fluid flux through the top or bottom reservoir boundaries because the overlying and underlying rock is assumed to be impermeable. Heat is conducted into the reservoir from the top and bottom boundaries according to a built-in TOUGH2 analytical function, which assumes Cartesian, one-dimensional heat conduction coming from the background, which is at temperature T_e , acting as a local heat source term (Pruess et al., 1999). The reservoir heat extraction working fluid is water.

The base case model parameters and assumptions are shown in Table 1 and are based on Adams et al. (2015). In Section 3.3, we also present results for a thin reservoir with a thickness of 30 m, one-tenth the base case reservoir thickness.

2.5. Estimating electricity generation

The power cycle generation model is adopted from Adams et al. (2015), follows the approach presented in Scenario 5 of that work which uses R245fa as the secondary working fluid for the indirect power system (Fig. 3), and uses the same parameter values as the base-case scenario from that work. The model essentially remains unchanged from the original work, except for two changes. First, Adams et al. (2015) used the TOUGH2 reservoir simulator for calculating reservoir impedance, while in this work, we utilize an analytical solution for reservoir impedance as described in Section 2.1. Second, wellbore heat loss from the production well (Section 2.2) was not considered in Adams et al.

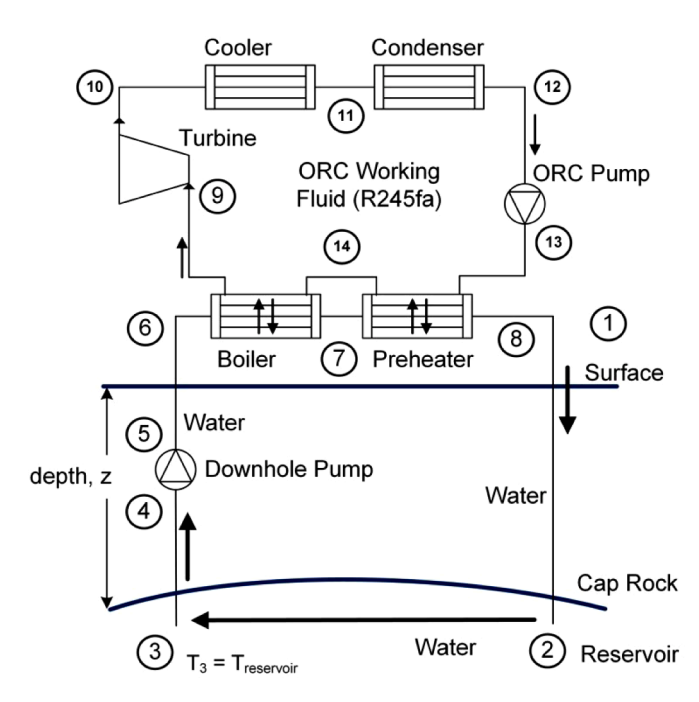


Fig. 3. Cycle schematics for an indirect (i.e., binary) groundwater - Organic Rankine Cycle (ORC) geothermal power plant. Modified from Adams et al. (2015).

(2015) but is included in our work here. Power generation is calculated without considering pressure depletion in the reservoir.

Fig. 3 shows the cycle schematics for the indirect (i.e., binary) water-Organic Rankine Cycle (ORC). In the lower loop, the primary fluid (water) is circulated from the land surface through the reservoir, where it gains heat; and back to the land surface, where it supplies heat to the secondary working fluid. In the upper loop, the organic secondary fluid (R245fa) is heated by the primary fluid via a heat exchanger, driving the ORC to produce electricity.

We include the most important aspects of the power cycle calculation in this section, but we encourage readers to refer Adams et al. (2015) for more information about the power cycle calculations. The flow rate through the primary loop is chosen to maximize the net power generation, which is the gross turbine power minus the parasitic power of the pumps and the heat rejection equipment. The mass flow rate through the secondary loop depends on the flow rate of the primary fluid so that all heat is transferred and a 7 $\,^\circ\mathrm{C}$ pinch point is obtained.

In the secondary cycle, the secondary fluid leaves the boiler at State 9 and is expanded through the turbine to State 10 with an assumed isentropic turbine efficiency of 80%. It is cooled isobarically to saturation at State 11. Going through the condenser towards the ORC pump (State 12), the R245fa fluid is cooled isobarically to 7 $^{\circ}\text{C}$ above the ambient temperature (i.e., a 7 $^{\circ}\text{C}$ approach temperature). The ORC pump efficiency is assumed to be 90%. The primary fluid is set to be at least 7 $^{\circ}\text{C}$ hotter than the secondary working fluid in the heat exchangers. Thus, the primary fluid temperature at States 7 and 8, are at least 7 $^{\circ}\text{C}$ above the boiling and condensing temperatures of R245fa.

The entire upper loop and portions of the lower loop are solved using MATLAB. For example, the pressure drop due to friction in the wellbore from Points 1 to 2 and 3 to 6 (Fig. 3) are solved with MATLAB. Likewise, all pressure and thermodynamic equations of the upper loop (Points 6 – 14) are solved with MATLAB, using the CoolProp thermodynamic property library (Bell et al., 2014). In contrast, the reservoir modeling aspects of our paper here are provided by Points 2–3 (Section 2.1, 2.3, and 2.4) and the wellbore heat loss is given by Points 3–6 (Section 2.2).

3. Results and discussion

In Section 3.1, we summarize the analytical reservoir impedance solutions and compare them to the numerical solution from TOUGH2, discussed in Section 2.4. In Section 3.2, we use the reservoir impedance from Section 2.1, the wellbore heat loss from Section 2.2, and the power cycle model from Section 2.5 to calculate the initial electric power generation. This power generation is compared to the power generation of the numerical reservoir simulator from Section 2.4. In Section 3.3, we compare reservoir heat depletion results from the analytical solution in Section 2.3 with the numerical model.

3.1. Reservoir impedance

The reservoir impedance solutions from Section 2.1 can be expressed more concisely. The solutions can be calculated as a function of the location of the well/porous medium interface (i.e., x_0 or r_0) and the cross-sectional area, A_c , and then expressed in terms of the constants C_1 and C_2 :

$$\frac{\Delta P_{tot}}{\dot{m}_{tot}} = \frac{2\overline{\mu}}{\overline{\rho}} \frac{1}{\kappa} \int_{x_0}^{\frac{1}{2}} \frac{dx}{A_c(x)} = \frac{\overline{\mu}}{\overline{\rho}} \frac{1}{\kappa b} C_1 \ln C_2$$
(37)

The solutions of Section 2.1 are summarized in Table 2, using the variables A_c , C_1 , C_2 , and x_0 or r_0 from Eq. (37). The final column shows the value of $C_1 \ln C_2$, which is proportional to the reservoir impedance, with an assumed value of L/D=1000. Notably, the differences in reservoir impedance are small amongst all analytical solutions (the range for $C_1 \ln C_2$ is 1.8 to 2.2), which indicates that the ID exhibits reservoir impedances that are not significantly different from those obtained for a 5-spot TDF. We suggest the use of the "TDF-Hybrid" solution (Eq. (14)) for 5-spot TDFs because it honors the radial fluid flow pattern near wells and the linear fluid flow pattern near the midpoint between an injection and a production well, at x = L/2, as discussed in Section 2.1.3. We suggest the use of the "ID-Potential" solution (Eq. (23), Section 2.1.4) for the ID cases, as it includes the entire sweep area.

In Fig. 4, we compare the reservoir impedance as a function of time for the numerical and two analytical solutions. The analytical results are provided by Eq. (14) for the 5-spot TDF-Hybrid and Eq. (23) for the "IDPotential". In the numerical model, fluid properties are pressure- and temperature-dependent, which is accounted for internally in TOUGH2. For the analytical solutions, the temperature from the reservoir heat depletion solution (Eq. (31)), and the hydrostatic pressure are inputs to the CoolProp (Bell et al., 2014) Python library, which calculates the fluid properties.

In all three solutions, the reservoir impedance increases with time due to the increase in the kinematic viscosity of the groundwater as the reservoir cools. The shapes of the impedance curves differ because of the viscosity calculation method. The numerical solution accounts for spatial and temporal viscosity variations as the reservoir cools. As the reservoir near the injection well starts cooling almost immediately upon water injection, the kinematic viscosity near the injection well increases

at early times. The reservoir impedance increases steadily throughout time as the cooled region grows. The reservoir impedance doubles by the tenth year of operation. In contrast, the analytical solution uses the average reservoir temperature and pressure to calculate the average kinematic viscosity of the water, which does not account for spatial variations in fluid properties. It thus takes approximately ten years in the analytical solution case for the average temperature to change by 10% (see Section 3.3). Thus, the average kinematic water viscosity and the average reservoir impedance have only increased by approximately 10% after ten years. In fact, the analytical solution shows that it takes about 200 years for the reservoir impedance double due to cooling.

The numerical solution gives a lower reservoir impedance than the two analytical solutions, which are similar to each other, differing by only 13%. At early times, when the fluid properties are in good agreement, the analytical solutions yield reservoir impedances that are roughly twice as high as those obtained by the numerical solution.

The discrepancies among the numerical and the analytical reservoir impedances may be partially explained by the employed grid resolution. Ravilov (2019) found that the reservoir impedance increases with the number of nodes in a reservoir simulator. Thus, the numerical solution in Fig. 4, with its relatively low spatial resolution, likely provides a lower bound for the reservoir impedance.

The Ravilov (2019) study raises an important consideration: mesh discretization can have a large effect on reservoir impedance in numerical simulations. In his study, as the number of nodes increased from 1300 to 600,000, the reservoir impedance increased by approximately 25% (from 38 to 48 kPa-s/kg). Through extrapolation, Ravilov (2019) predicted that an infinite number of nodes would lead to an impedance increase of approximately 50% (to 58 kPa-s/kg). It is difficult to know if the impedance asymptotes to a fixed value as the number of nodes goes to infinity, and if this asymptote does exist, it is also difficult to know what the value of this impedance will be. Ravilov's (2019) work suggests that getting an accurate reservoir impedance value using a numerical simulator may require nearly infinite computational resources.

It is difficult to say whether the analytical or the numerical reservoir impedance solutions are more accurate. Each calculation method has its strengths and weaknesses and may be useful depending on the problem of interest. The analytical approach is computationally less expensive than the numerical approach. On the other hand, the analytical solution relies on simplifications, such as the use of average fluid properties, a one-dimensional coordinate system, and a uniform fluid flow field. The numerical simulation does not rely on these simplifications but depends on the spatial resolution of the computation mesh, as discussed in the previous paragraph. Moreover, the analytical and numerical solutions only differ by roughly a factor of two, which is often much smaller than other uncertainties associated with subsurface reservoir properties, such as reservoir transmissivity. Reservoir transmissivity can exhibit uncertainties that are on the order of a magnitude or more, particularly if a geothermal reservoir has not been thoroughly characterized or is highly heterogeneous.

Table 2 Analytical impedance, right-most column indicates value for L = 1000D.

Well pattern	x_0 or r_0	A_c	C_1	C_2	$C_1 ln C_2$
TDF-cartesian (Section 2.1.1, Eq. (8))	πD	2xb	1_	<u>4</u> <u>L</u>	1.8
ID-radial (Section 2.1.2, Eq. (12))	8 D	$2\pi rb$	4 1	$_{L}^{\pi \;D}$	2.2
TDF-hybrid (Section 2.1.3, Eq. (14))	$\frac{\overline{2}}{D}$	$2b \left(2\left(-\frac{\pi}{2}\right) \right) L\pi$	$\frac{\pi}{\pi}$	$rac{\overline{D}}{\pi}$ L	2.1
	$\overline{2}$	$\frac{2b}{\frac{L}{2}-x_o}\left(x^2\left(1-\frac{\pi}{4}\right)+x(\frac{L\pi}{8}-x_o)\right)$	$\frac{-}{\pi}$	$\overline{4} \overline{D}$	
ID-potential (Section 2.1.4, Eq. (23))	<u>D</u>	$2 \cdot \pi \cdot b$	<u>1</u>	<u>L</u>	1.9
	2	$(rac{1}{r^2} - rac{2}{L \cdot r})^{1/2}$	π	De	

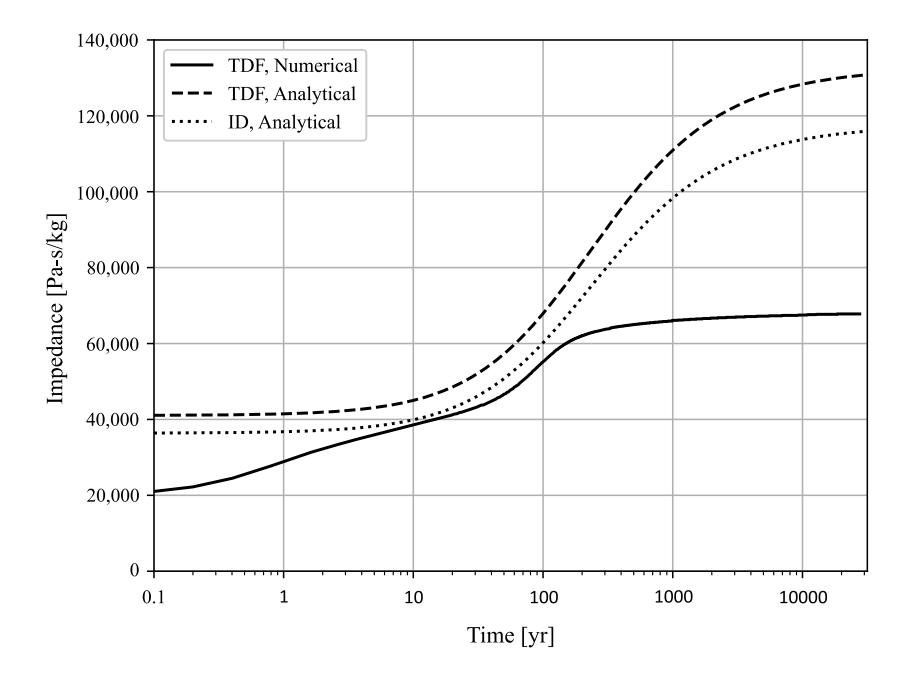


Fig. 4. The TDF numerical solution using TOUGH2, the TDF analytical solution using the "TDF-Hybrid" approach, and the ID analytical solution using the "ID-Potential" approach.

3.2. Electric power generation

Fig. 5a shows electric power generation as a function of reservoir transmissivity for various reservoir impedance models. There are little differences in electric power generation (<10%) among the four analytical reservoir impedance models, as the differences in the underlying analytical reservoir impedance calculations are small (<18%). However, the reservoir impedance predicted by the numerical model is roughly half of the reservoir impedance predicted by the analytical solutions for a given reservoir transmissivity value. This reservoir impedance difference results in up to twice the predicted electric power generation when a numerical reservoir impedance model is used, compared to using an analytical reservoir impedance model. As was stated in Section 3.1, the numerical and the analytical solutions yield a range of possible reservoir impedances, and it is unclear which calculation method yields more accurate results. In many applications, the uncertainty in the reservoir transmissivity may be much larger than the uncertainty introduced by the reservoir impedance calculation method. Thus, to calculate electric power generation accurately, it is crucial to reduce the uncertainties as much as possible in the reservoir transmissivity. However, there will likely always remain a significant uncertainty in the prediction of heat and electric power generation, particularly before reservoir impedance has been measured in the field.

The difference in predicted electric power generation is minor between models that include wellbore heat loss and those that neglect it, as shown in Fig. 5b. At low reservoir transmissivities (<3200 mD-m), the production temperature is different between models with and without wellbore heat loss. However, at low reservoir transmissivities, electric power generation is negligible (<0.2 MWe), and therefore the absolute difference in electricity generation is also very small. As the reservoir transmissivity increases, the production temperature in the wellbore heat loss model asymptotes to the production temperature in the adiabatic wellbore model. Therefore, the percentage difference in electric power generation between the models is very small for hightransmissivity reservoirs. Note that we do not show the brine mass flow rate or the thermal output in Fig. 5. However, at high reservoir transmissivities (>10,000 mD-m), the production temperature is approximately constant (i.e., it asymptotes to the reservoir temperature). Therefore, both the mass flow rate and the thermal output are proportional to the electric power generation, following an "S" shape on the right side of Fig. 5(b). Since the difference in predicted power generation is small across the full range of reservoir transmissivities, wellbore heat loss can typically be neglected in many simulations of geothermal energy extraction from sedimentary basin reservoirs.

3.3. Reservoir heat depletion

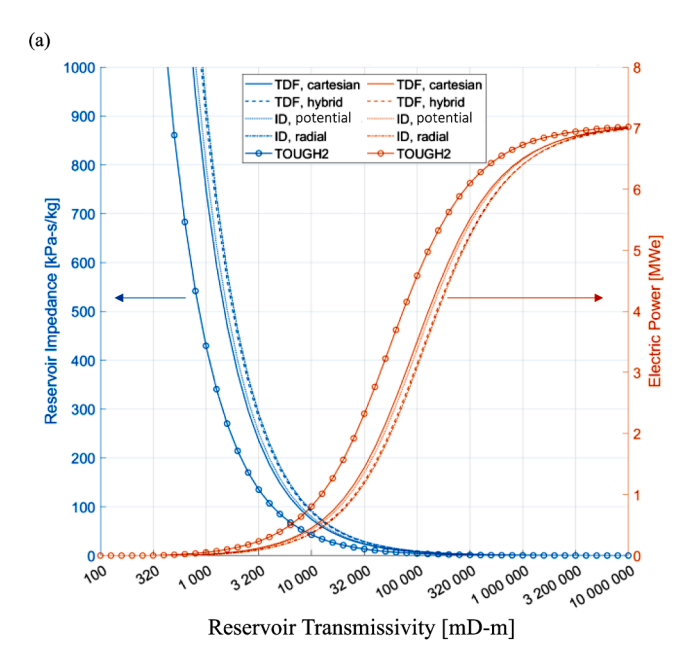
As the temperature of a reservoir reduces, so does the power generation from the reservoir. Therefore, understanding the reservoir temperature as a function of time offers insights into power generation as a function of time and reservoir heat depletion.

Fig. 6 shows the non-dimensional reservoir temperature versus time for both the analytical and the numerical solutions, calculated from Eq. (31) (for analytical) and in a post-processing step from the numerical solution. The solutions that neglect heat conduction (dotted lines in Fig. 6) are calculated from Eq. (33). Fig. 6a uses the logarithm of time to illustrate the late-time behavior, while Fig. 6b uses a linear time scale to emphasize the shape of the curves at early times and how (in)significant the inclusion of heat conduction from the reservoir-surrounding rock into the reservoir is, for determining the reservoir temperature.

3.3.1. Comparison of solutions

The shapes of the analytical and the numerical solutions are different, which is partially the result of them representing the temperature at different locations in the reservoir. The analytical solution shows the average temperature of the reservoir, which always decreases at a decreasing rate. In contrast, the numerical solution shows the production well temperature, which decreases at an increasing rate until the cold front reaches the production well. Then the fluid production temperature continues to decrease, but at a decreasing rate. This temperature versus time pattern in the numerical solution is a classic example of so-called cold front breakthrough.

Another difference in the solutions is caused by the way in which heat is removed from the reservoir. In the analytical solution, heat is removed at a constant rate. In the numerical solution, a fluid flow rate and a fluid injection temperature are specified, such that the initial heat removal rate matches the rate in the analytical solution. However, as the reservoir cools, the heat removal rate decreases in the numerical



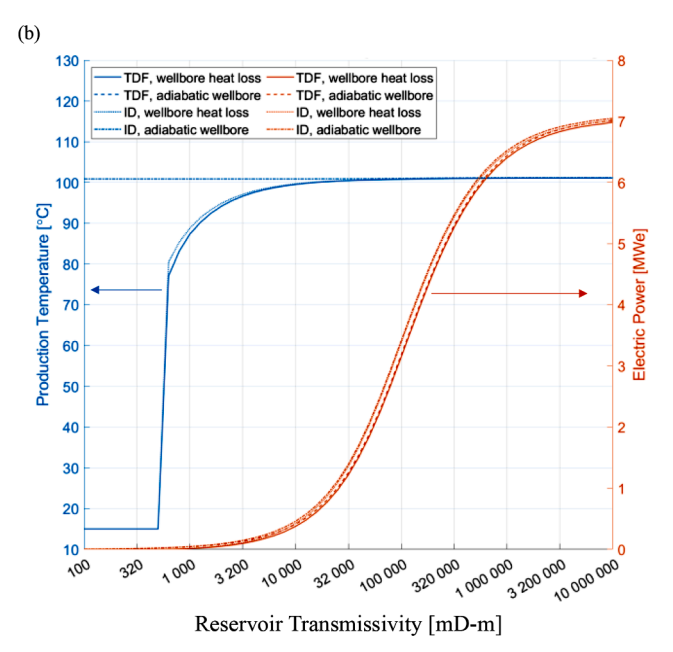


Fig. 5. Panel (a) shows reservoir impedance and electric power generation as a function of reservoir transmissivity and illustrates the sensitivity of power generation to the impedance model used, indicated by different line types (see legend). Panel (b) shows the production temperature and electric power generation as a function of reservoir transmissivity and illustrates the sensitivity of power generation to the assumptions made concerning wellbore heat loss, indicated by different line types (see legend). Both panels show four analytical reservoir impedance models and Panel (a) also shows the numerical reservoir impedance model. Horizontal arrows associate the curve with the related y-axis.

solution. The numerical solution may be more realistic for sedimentarybasin geothermal systems in this regard, whereas the analytical solution represents a worst-case (i.e., cold) bound for heat depletion, especially at later energy production times.

The numerical and the analytical model also differ in their respective problem geometries. The numerical solution uses a three-dimensional geometry, employing one-dimensional, cartesian heat conduction from above and from below the reservoir. In contrast, the analytical solution follows a one-dimensional radial heat flow geometry, where the

equivalent radius is adjusted to match the volume and the surface area of the numerical solution (Section 2.3).

Despite the differences discussed in the previous paragraphs, both the analytical and the numerical solutions describe a reservoir's heat depletion with the same available reservoir volume and amount of removable heat. Heat conduction into the reservoir from outside is treated similarly in that they both use one-dimensional analytical approaches (recall from Section 2.4 that in the numerical simulator the conduction of heat into the reservoir is an analytical solution that is built into TOUGH2). Thus, it is possible to get an estimate of reservoir heat depletion employing both the numerical and the analytical approaches.

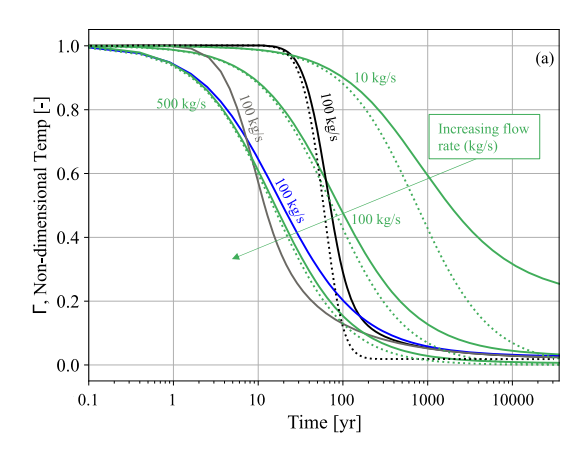
The analytical solution can be used in at least two ways. Firstly, it can be interpreted as the average reservoir temperature. In this approach, it always provides a lower-bound on the average reservoir temperature due to its assumed constant rate of heat removal, as discussed earlier in this section. Secondly, the analytical solution can be interpreted as the production temperature used for power generation calculations. When following this interpretation, the analytical solution is conservative at early times, as it predicts a temperature that is lower than the production temperature provided by the numerical solution. While a numerical solution would likely be more accurate for power generation calculations, it is computationally expensive, which may be why some previous studies have neglected reservoir heat depletion and only reported the initial power generation (e.g., Randolph and Saar, 2011; Adams et al., 2015). Using the analytical solution for reservoir temperature provides a computationally inexpensive lower bound, which could prove to be useful in combination with electric power cycle models to calculate power generation over a geothermal field's lifetime.

3.3.2. Physical insights into heat depletion and conduction

Fig. 6a shows different fluid flow rates and their effects on the analytical solution. For high fluid flow rates, the reservoir temperature decreases faster, and steady-state conditions are achieved earlier, reaching lower temperatures. However, for lower fluid flow rates, the reservoir temperature decreases more slowly and approaches a steady state (greater than T_{inj}) at much later times because heat conduction brings heat into the reservoir at the same rate as the working fluid removes it. In contrast, the analytical solutions that do not consider heat conduction all approach T_{inj} ($\Gamma=0$) at earlier times because there is no heat recharge.

Heat conduction affects the reservoir temperature more significantly in reservoirs that exhibit lower fluid flow rates, as shown by the curves that represent 10~kg/s, 100~kg/s, and 500~kg/s in Fig. 6a. At 10~kg/s, there is a large difference between the temperatures with (solid green curve) and without (dashed green curve) heat conduction. However, this difference is minor for the 100~kg/s curves and barely perceptible in the 500~kg/s curve.

Fig. 6b compares the base case (reservoir thickness = 300 m) with a mass flow rate equal to 100 kg/s to a thin reservoir (thickness = 30 m) with the same mass flow rate, highlighting the effect of reservoir size and aspect ratio on reservoir heat depletion and on the importance of heat conduction. For this discussion, we assume that the reservoir lifetime ends when 20% of the original heat is depleted from the reservoir, which corresponds to $\Gamma=0.8$ and $T_r=86.4$ °C. While our assumption that 20% heat depletion corresponds to the end of a reservoir's life is somewhat arbitrary, it allows for comparison of reservoir lifetime for different reservoir thickness and conduction from surrounding rock. However, it is possible to run the same analysis with a different definition of the reservoir lifetime. One takeaway is that the base-case reservoir has a longer lifetime than the thin reservoir because there is more heat initially in the base case reservoir. The base case reservoir takes between 20 and 44 years, depending on the solution utilized (see the green and black curves in Fig. 6b), to reach the end of its lifetime. In contrast, this occurs in less than six years for the thin reservoir (see the blue and gray curves in Fig. 6b). Secondly, heat conduction plays a larger role in extending the reservoir lifetime for a thin reservoir than for



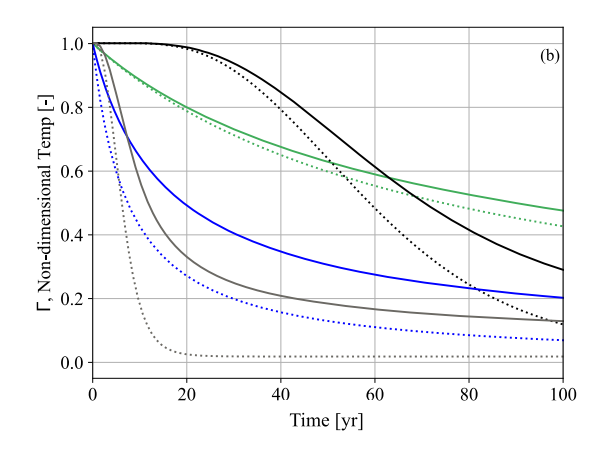


Fig. 6. (a) Analytical versus numerical solutions of normalized reservoir temperature w.r.t. logarithm of time for different fluid mass flow rates and different reservoir thicknesses. (b) Normalized reservoir temperature versus time for a fluid mass flow rate equal to 100 kg/s. Dotted lines indicate scenarios that do not include heat conduction from the surrounding to the reservoir. The base-case reservoir (represented by green and black curves) is 300 m thick, and the thin reservoir (represented with blue and gray curves) is 30 m thick. The non-dimensional temperature, Γ, is defined in Eq. (31), where $\Gamma = 1$ corresponds to $T_r = T_e = 102.5$ °C; $\Gamma = 0.8$ corresponds to 20% heat depletion, which we assume marks the end of the reservoir lifetime with $T_r = 86.4$ °C; and $\Gamma = 0$ corresponds to $T_r = T_{inj} = 22$ °C. For more information on heat depletion and reservoir lifetimes, please see Adams et al. (2021).

the thicker base-case reservoir. For example, in the analytical solution (green curves in Fig. 6b), heat conduction extends the base-case reservoir lifetime by 7%, from 18.6 years, without heat conduction (dashed green curve), to 20.0 years, with heat conduction (solid green curve). In contrast, heat conduction extends the thin reservoir lifetime by 140%, from 1.8 years without heat conduction (dashed blue line), to 4.3 years with heat conduction (solid blue line). Thus, as expected, heat conduction affects reservoirs with a high surface area to volume ratio more significantly than reservoirs with an inverse ratio.

4. Conclusions

This paper introduced and used analytical solutions to approximate the impedance, wellbore heat loss, and heat depletion of geothermal reservoirs under energy production. The reservoir impedance and wellbore heat loss solutions were coupled to a power cycle model to calculate electric power generation. The reservoir heat depletion solution gave insights about power generation decline and reservoir lifetime. Key takeaways include:

- 1. The utility of the analytical impedance solution relative to the numerical impedance solution depends on the assumptions and the application. In this work, the analytical solution provided a reservoir impedance that was higher than the reservoir impedance provided by the numerical solution, and thus resulted in less estimated electricity generation. But the results of the numerical solution depend on the resolution of the grid used in the simulation, which can produce results that vary substantially (Section 3.1). In contrast, analytical solutions are independent of grid resolution and computationally inexpensive, but rely on simplifications (e.g., average fluid properties and uniform fluid velocity profiles). Considering the pros and cons of both types of solutions, we consider both approaches as acceptable, depending on the application, particularly for exploration studies, where screening-level calculations are performed. Uncertainty due to differences between the analytical and the numerical values for reservoir impedance are likely much smaller than other subsurface uncertainties in an insufficiently characterized geological system. Among the analytical solutions, we recommend the use of the "ID-Potential" solution (Eq. (23)) for IDs and the "TDF-Hybrid" solution (Eq. (14)) for 5-spot TDFs.
- 2. Wellbore heat losses may be neglected for many calculations of geothermal electric power generation (Fig. 5b). For high reservoir transmissivities, the fluid flow rate was large enough so that the fluid

- production temperature depletion was insignificant and power generation was similar for calculations with and without wellbore heat loss. For low-transmissivity reservoirs (<3200 mD-m), the fluid flow rate was low, which resulted in little electricity generation (<0.2 MW_e), with or without wellbore heat loss.
- 3. The analytical and numerical solutions of the reservoir heat depletion provide temperatures at different regions of the reservoir, but fundamentally they both reflect the temperature of reservoirs with the same initial amount of removable heat, which is replenished by heat conduction from the surroundings. The analytical solution (Eq. (31)) represents a lower bound of the average reservoir temperature for all time (particularly at later times) and represents a lower bound on the production temperature during early years (Section 3.3). Coupling the analytical heat depletion solution with a power cycle model can be computationally inexpensive way to calculate the electric power generation of the lifetime of a geothermal power plant.
- 4. The amount of heat initially present in the reservoir is closely related to the reservoir size and can be approximated by a lumped mass, with (Eq. (31)) or without (Eq. (33)) considering heat conduction. The thin reservoir reached 20% heat depletion faster than the thick reservoir, as expected. For the thin reservoir, all approaches (analytical and numerical with and without heat conduction with 100 kg/s flow rate) predicted <6 years before 20% heat depletion was reached, whereas for the thicker, base-case reservoir, all approaches predict between 19 and 44 years before 20% heat depletion was reached.
- 5. Reservoir temperature is more sensitive to heat conduction from the surroundings in scenarios with low fluid flow rates (Fig. 6a) or a high ratio of reservoir surface area to volume (e.g., the thin reservoir in Section 3.3).

There are advantages and disadvantages of using analytical versus numerical reservoir models. A careful weighing of objectives should be made when constructing a geothermal power plant model that couples reservoir performance with electricity generation. Some of the conclusions above can provide guidance when weighing these objectives. Others offer insights into the behavior of geothermal reservoirs and power production.

CRediT authorship contribution statement

Daniel T. Birdsell: Conceptualization, Methodology, Software, Validation, Visualization, Writing – original draft, Writing – review & editing. **Benjamin M. Adams:** Conceptualization, Methodology, Software, Validation, Visualization, Writing – original draft, Writing –

review & editing. Paromita Deb: Formal analysis, Project administration, Writing – original draft, Writing – review & editing. Jonathan D. Ogland-Hand: Writing – original draft, Writing – review & editing. Jeffrey M. Bielicki: Writing – review & editing. Mark R. Fleming: Writing – review & editing. Martin O. Saar: Funding acquisition, Writing – review & editing.

Declaration of Competing Interest

The authors declare that they have no known competing financial interests or personal relationships that could have appeared to influence the work reported in this paper.

Data availability

Input file for the numerical model is shared as supplementary information.

Acknowledgement

We thank the Werner Siemens Foundation (Werner Siemens-Stiftung) for its support of the Geothermal Energy and Geofluids (GEG.ethz.ch) Group at ETH Zurich, Switzerland. We also thank Dr. Anozie Ebigbo at Helmut Schmidt University for his generous time contribution and consultation regarding the reservoir impedance derivations and Qingrun Yang of the Ohio State University for useful discussions about the reservoir heat depletion solution.

ACT ELEGANCY, Project No 271498, has received funding from DETEC (CH), FZJ/PtJ (DE), RVO (NL), Gassnova (NO), BEIS (UK), Gassco AS and Statoil Petroleum AS, and is cofounded by the European Commission under the Horizon 2020 program, ACT Grant Agreement No 691712.

This work was also supported by HEATSTORE (170153-4401), which has been subsidized through the ERANET cofund GEOTHERMICA (Project n. 731117), from the European Commission, RVO (the Netherlands), DETEC (Switzerland), FZJ-PtJ (Germany), ADEME (France), EUDP (Denmark), Rannis (Iceland), VEA (Belgium), FRCT (Portugal), and MINECO (Spain).

JB also acknowledges the U.S. National Science Foundation Innovations at the Nexus of Food, Energy, and Water Systems (INFEWS) program (1739909), the U.S. National Science Foundation National Research Traineeship Program (1922666), and the Alfred P. Sloan Foundation's Net-Zero and Negative Emissions Technologies program (grant no. 2020–12,466).

Supplementary materials

Supplementary material associated with this article can be found, in the online version, at doi:10.1016/j.geothermics.2023.102843.

References

- Adams, B.M., Kuehn, T.H., Bielicki, J.M., Randolph, J.B., Saar, M.O., 2014. On the importance of the thermosiphon effect in CPG (CO₂ plume geothermal) power systems. Energy 69, 409–418. https://doi.org/10.1016/j.energy.2014.03.032.
- Adams, B.M., Kuehn, T.H., Bielicki, J.M., Randolph, J.B., Saar, M.O., 2015. A comparison of electric power output of CO₂ Plume Geothermal (CPG) and brine geothermal systems for varying reservoir conditions. Appl. Energy 140, 365–377. https://doi. org/10.1016/j.apenergy.2014.11.043.
- Adams, B.M., Vogler, D., Kuehn, T.H., Bielicki, J.M., Garapati, N., Saar, M.O., 2021. Heat depletion in sedimentary basins and its effect on the design and electric power output of CO₂ plume geothermal (CPG) systems. Renew. Energy. https://doi.org/ 10.1016/j.renene.2020.11.145.
- Agemar, T., Weber, J., Schulz, R., 2014. Deep geothermal energy production in Germany. Energies 7, 4397–4416. https://doi.org/10.3390/en7074397.
- Arslan, O., 2011. Power generation from medium temperature geothermal resources: ANN-based optimization of Kalina cycle system-34. Energy 36 (5), 2528–2534. https://doi.org/10.1016/j.energy.2011.01.045.

Bakker, M., Strack, O.D., 1996. Capture zone delineation in two-dimensional groundwater flow models. Water Resour. Res. 32 (5), 1309–1315.

- Banks, J., Harris, N.B., 2018. Geothermal potential of foreland basins: a case study from the western Canadian sed basin. Geothermics 76, 74–92. https://doi.org/10.1016/j. geothermics.2018.06.004.
- Bell, I.H., Wronski, J., Quoilin, S., Lemort, V., 2014. Pure and pseudo-pure fluid thermophysical property evaluation and the open-source thermophysical property library CoolProp. Ind. Eng. Chem. Res. 53 (6), 2498–2508.
- Birdsell, D.T., Adams, B.M., Saar, M.O., 2021. Minimum transmissivity and optimal well spacing and flow rate for high-temperature aquifer thermal energy storage. Appl. Energy 289, 116658.
- Boissavy, C., Henry, L., Genter, A., Pomart, A., Rocher, P. and Schmidle-Bloch, V. (2019). Geothermal energy use, country update for France. Proceedings European Geothermal Congress 2019. 11-14 June 2019, The Hague, The Netherlands.
- Carslaw, H.S., Jaeger, J.C., 1986. Ch. 13 The Laplace transformation: problems on the cylinder and sphere. Conduction of Heat in Solids Second Edition. Clarendon Press, Oxford, pp. 349–350.
- Clauser, C. (2006). Ch.8 geothermal energy, In: Heinloth, K. (ed), Landolt-Börnstein, Group VIII: Advanced Materials and Technologies, Vol. 3: Energy Technologies, Subvol. C: Renewable Energies, Springer Verlag, Heidelberg-Berlin, 493–604.
- Colonna, P., Casati, E., Trapp, C., Mathijssen, T., Larjola, J., Turunen-Saaresti, T., Uusitalo, A., 2015. Organic rankine cycle power systems: from the concept to current technology, applications, and an outlook to the future. ASME. J. Eng. Gas Turbines Power 137 (10), 100801. https://doi.org/10.1115/1.4029884.
- Dawo, F., Fleischmann, J., Kaufmann, F., Schifflechner, C., Eyerer, S., Wieland, C., Spliethoff, H., 2021. R1224yd(Z), R1233zd(E) and R1336mzz(Z) as replacements for R245fa: experimental performance, interaction with lubricants and environmental impact. Appl. Energy 288, 116661. https://doi.org/10.1016/j. apenergy.2021.116661.
- Deb, P., Knapp, D., Marquart, G., Clauser, C., Trumpy, E., 2020. Stochastic workflows for the evaluation of EGS potential in geothermal greenfields with sparse data: the case study of Acoculco, Mexico. Geothermics 88, 101879. https://doi.org/10.1016/j. geothermics.2020.101879.
- Eyerer, S., Wieland, C., Vandersickel, A., Spliethoff, H., 2016. Experimental study of an ORC (Organic Rankine Cycle) and analysis of R1233zd-E as a drop-in replacement for R245fa for low temperature heat utilization. Energy 103, 660–671. https://doi. org/10.1016/j.energy.2016.03.034.
- Eyerer, S., Dawo, F., Kaindl, J., Wieland, C., Spliethoff, H., 2019. Experimental investigation of modern ORC working fluids R1224yd(Z) and R1233zd(E) as replacements for R245fa. Appl. Energy 240, 946–963. https://doi.org/10.1016/j. apenergy.2019.02.086.
- Ezekiel, J., Adams, B.M., Saar, M.O., Ebigbo, A., 2022. Numerical analysis and optimization of the performance of CO₂-Plume Geothermal (CPG) production wells and implications for electric power generation. Geothermics 98, 102270. https:// doi.org/10.1016/j.geothermics.2021.102270.
- Ge, S., Saar, M.O., 2022. Review: induced seismicity during geoenergy development a hydromechanical perspective. J. Geophys. Res. (JGR): Solid Earth 127, e2021JB023141. https://doi.org/10.1029/2021JB023141.
- Goldbrunner, J. and Goetzl, G. (2019). Geothermal energy use, country update for Austria. *Proceedings European Geothermal Congress 2019. 11-14 June 2019*, The Hague, The Netherlands.
- Huenges, E., 2016. 25 enhanced geothermal systems: review and status of research and development. In: DiPippo, R. (Ed.), Geothermal Power Generation. Woodhead Publishing, pp. 743–761.
- Langella, G., Paoletti, V., DiPippo, R., Amoresanoa, A., Steinunnard.ttir, K., Milano, M, 2017. Krafla geothermal system, northeastern Iceland: performance assessment of alternative plant configurations. Geothermics 169, 74–92. https://doi.org/10.1016/i.geothermics.2017.04.001.
- Link, K. and Minnig, C. (2022). Geothermal energy use, country update for Switzerland. Proceedings European Geothermal Congress 2022. 17-21 October 2022. Berlin, Germany.
- Lüschen, E., Wolfgramm, M., Fritzer, T., Dussel, M., Thomas, R., Schulz, R., 2014. 3D seismic survey explores geothermal targets for reservoir characterization at Unterhaching, Munich, Germany. Geothermics 50, 167–179. https://doi.org/10.1016/j.geothermics.2013.09.007.
- Moeck, I.S., Dussel, M., Weber, J., Schintgen, T., Wolfgramm, M., 2019. Geothermal play typing in Germany, case study Molasse Basin: a modern concept to categorise geothermal resources related to crustal permeability. Neth. J. Geosci. 8, e14. https:// doi.org/10.1017/njg.2019.12.
- Minissale, A., 1991. The Larderello geothermal field: a review. Earth Sci. Rev. 31, 133–151. https://doi.org/10.1016/0012-8252(91)90018-B.
- Moya, D., Akinsipe, O.C., Kaparaju, P., et al., 2021. Various cycle configurations for geothermal power plants. In: Colpan, C.O., et al. (Eds.), Thermodynamic Analysis and Optimization of Geothermal Power Plants. Elsevier, pp. 3–15. https://doi.org/ 10.1016/B978-0-12-821037-6.00005-6.
- Nathenson, M., Guffanti, M., 1988. Geothermal gradients in the conterminous United States. J. Geophys. Res. 93 (B6), 6437–6450. https://doi.org/10.1029/ JB093iB06p06437.
- Nordbotten, J.M., Celia, M.A., 2012. Geological Storage of CO₂: Modeling approaches for Large-Scale Simulation. John Wiley and Sons, Hoboken, NJ, USA, p. 2012.
- Pruess, K., 2004. The TOUGH codes A family of simulation tools for multiphase flow and transport processes in permeable media. Vadose Zone J. 3, 738–746.
- Pruess, K., 2005. ECO2N: a TOUGH2 fluid Property Module for Mixtures of Water, NaCl, and CO₂. Rep. LBNL-57952. Lawrence Berkeley National Laboratory, Berkeley.
- Pruess, K., 2006. Enhanced geothermal systems (EGS) using $\rm CO_2$ as working fluid—a novel approach for generating renewable energy with simultaneous sequestration of

- carbon. Geothermics 35, 351–367. https://doi.org/10.1016/j.geothermics.2006.08.002.
- Pruess, K., Moridis, G., Oldenburg, C., 1999. TOUGH2 User's guide, Version 2.0. Lawrence Berkeley National Laboratory, Berkeley. Report LBNL-43134.
- Randolph, J.B., Saar, M.O., 2011. Combining geothermal energy capture with geologic carbon dioxide sequestration. Geophys. Res. Lett. 38, L10401. https://doi.org/ 10.1029/2011GL047265.
- Ravilov, M., 2019. Master Thesis. ETH Zurich. https://doi.org/10.3929/ethz-b-000387209
- Siebt, P., Kabus, F. and Hoth, P. (2005). The Neustadt-Glewe Geothermal Power Plant practical experience in the reinjection of cooled thermal waters into sandstone aquifers. Proceedings World Geothermal Congress 2005, Antalya, Turkey, 24–29 April 2005, Antalya, Turkey.
- Strack, O.D., 1999. Principles of the analytic element method. J. Hydrol. (Amst.) 226 (3–4), 128–138.
- Stern, F., 2006. Mechanics of Fluids and Transport Processes Lecture Notes. https://user.engineering.uiowa.edu/~fluids/Posting/Lecture_Notes/Chapter6_Potential_Flow.pdf.
- Tartière, T., Astolfi, M., 2017. A world overview of the organic rankine cycle market. Energy Procedia 129, 2–9. https://doi.org/10.1016/j.egypro.2017.09.159.
- Weber, J., Born, H., Pester, S., Moeck, I., 2021. Geothermal energy use in Germany, country update 2015-2019. In: Proceedings World Geothermal Congress 2020+1, April October 2021. Reykjavik, Iceland.
- Zhang, Y., Pan, L., Pruess, K., Finsterle, S., 2011. A time-convolution approach for modelling heat exchange between a wellbore and surrounding formatioon. Geothermics 40, 261–266.